



Identification of individual and few layers of WS₂ using Raman Spectroscopy

SUBJECT AREAS:

TWO-DIMENSIONAL MATERIALS

COMPUTATIONAL NANOTECHNOLOGY

NANOPARTICLES

SURFACES, INTERFACES AND THIN FILMS

Received
12 December 2012

Accepted
15 April 2013

Published
30 April 2013

Correspondence and requests for materials should be addressed to M.T. (mut11@psu.edu)

* These authors contributed equally to this work.

† Current address:
Department of Physics & Astronomy,
University of Louisville,
Louisville, KY 40292
USA.

‡ Current address:
On leave from Advanced Materials Department, IPICYT,
Camino a Presa San José 2055, Col. Lomas 4a Sección, San Luis Potosí, México.

Ayse Berkdemir^{1*}, Humberto R. Gutiérrez^{1*†}, Andrés R. Botello-Méndez², Néstor Perea-López¹, Ana Laura Elías¹, Chen-Ing Chia¹, Bei Wang¹, Vincent H. Crespi¹, Florentino López-Urías^{1‡}, Jean-Christophe Charlier², Humberto Terrones¹ & Mauricio Terrones^{1,3}

¹Department of Physics and Center for 2-Dimensional and Layered Materials, The Pennsylvania State University, University Park, PA 16802, USA, ²Institute of Condensed Matter and Nanosciences (IMCN), Université catholique de Louvain (UCL), Chemin des étoiles 8, 1348 Louvain-la-Neuve, Belgium, ³Department of Materials Science and Engineering and Materials Research Institute, The Pennsylvania State University, University Park, PA 16802, USA & Research Center for Exotic Nanocarbons (JST), Shinshu University, Wakasato 4-17-1, Nagano 380-853, Japan.

The Raman scattering of single- and few-layered WS₂ is studied as a function of the number of S-W-S layers and the excitation wavelength in the visible range (488, 514 and 647 nm). For the three excitation wavelengths used in this study, the frequency of the A_{1g}(Γ) phonon mode monotonically decreases with the number of layers. For single-layer WS₂, the 514.5 nm laser excitation generates a second-order Raman resonance involving the longitudinal acoustic mode (LA(M)). This resonance results from a coupling between the electronic band structure and lattice vibrations. First-principles calculations were used to determine the electronic and phonon band structures of single-layer and bulk WS₂. The reduced intensity of the 2LA mode was then computed, as a function of the laser wavelength, from the fourth-order Fermi golden rule. Our observations establish an unambiguous and nondestructive Raman fingerprint for identifying single- and few-layered WS₂ films.

Individual monolayers of transition metal dichalcogenides such as MoS₂ and WS₂ have recently caught the attention of the scientific community because these 2-dimensional semiconductors could have properties more attractive for specific applications than those of graphene^{1,2} and boron nitride^{3,4}. A single layer of MX₂ [M = (Mo or W) and X = (S, Se or Te)] typically contains one atomic layer of metal atoms with 6-fold in-plane coordination, hexagonally packed between two trigonal atomic layers of chalcogenide atoms. In single-layer form, the absence of interlayer coupling plus the lack of inversion symmetry (for supported films) leads to optical and electronic properties that differ markedly from those of the bulk^{5–9}. For example, the electronic band structure transitions from an indirect gap (in the bulk) to a direct gap in the monolayer⁷, and valley polarization (i.e. “valleytronics”) can be induced in monolayer MoS₂ by circularly polarized light^{10,11}. While MoS₂ has received copious attention in the search for new properties and potential applications of 2D semiconductors^{8,9,12–19}, little attention has been paid to monolayer and few-layer WS₂. In this respect, we have recently demonstrated the synthesis of single-layer WS₂ triangular islands and observed intense room-temperature photoluminescence (PL) associated with specific edges²⁰. Although Raman spectroscopy has become a very powerful tool for studying graphene^{21–23} and MoS₂^{13,17–19,24,25}, the Raman scattering of single- and few-layered WS₂ still remains largely unexplored. Raman spectroscopy can not only be used to identify the number of layers^{13,21,22,25,26}, but also probe subtle details in the electronic band structure and phonon dispersion through resonant Raman scattering^{21,27}. Here we provide the first systematic study of the Raman response in monolayer and few-layer WS₂ as a function of the laser excitation wavelength. We report a novel resonant second-order Raman feature in single-layered WS₂ and discuss the general characteristics of the phonon modes that can provide a fingerprint for monolayer WS₂.

Results

As previously reported²⁰, the synthesis of single- and few-layered WS₂ triangular 2D islands follows a two-step approach of thermal evaporation of tungsten trioxide (WO₃) followed by sulfurization (see Methods section). The sample morphology, crystal structure and chemical composition were studied by means of scanning and transmission electron microscopy (SEM, TEM) (Figures 1a–c)²⁰. Electron diffraction (inset in Figure 1b) reveals large single crystal domains with a high degree of crystallinity. Atomic force microscopy (AFM) was used to



determine the number of layers within these WS_2 triangular islands (Figures 1d). We extracted the thickness and wavelength-dependent behavior of the lattice vibrations in these 2D islands by correlating AFM images with Raman spectroscopy maps.

Raman spectra for bulk (i.e. multi-layered) WS_2 and MoS_2 have been previously studied. In a backscattering geometry, these spectra include first-order modes at the Brillouin zone center ($E_{2g}^1(\Gamma)$ and $A_{1g}(\Gamma)$) plus a zone-edge mode – activated by disorder – which has been identified as the longitudinal acoustic mode at the M point, $\text{LA}(\text{M})$. The longitudinal acoustic phonons $\text{LA}(\text{M})$ are in-plane collective movements of the atoms in the lattice, similar to the sound waves. They are periodic compressions and expansions of the lattice that occur along the direction of propagation. The symbol (M) refers to the specific direction and magnitude of the momentum \mathbf{q} of the phonon; in the phonon dispersion (frequency vs. momentum), they appear at the M-point of the Brillouin zone. Additional peaks correspond to multi-phonon combinations of these modes^{28–30}. Previous reports on monolayer MoS_2 and chemically exfoliated WS_2 ¹⁴ have focused exclusively on the first-order $E_{2g}^1(\Gamma)$ and $A_{1g}(\Gamma)$ optical modes. Resonant Raman scattering in single-layered dichalcogenides has not previously been observed.

Figures 1e and f show typical Raman spectra of monolayer WS_2 regions using 514.5 nm and 488 nm excitations. For $\lambda_{\text{exc}} = 488 \text{ nm}$, the Raman spectrum is dominated by the first-order modes: $\text{LA}(\text{M})$

at 176 cm^{-1} , $E_{2g}^1(\Gamma)$ at 356 cm^{-1} and $A_{1g}(\Gamma)$ at 418 cm^{-1} . However, when monolayer WS_2 is excited at 514.5 nm, the Raman spectrum becomes very rich, revealing many second-order peaks that are stronger than those observed in the bulk material. Figures 1e and 1f give symmetry assignments for several peaks according to previous reports in bulk and fullerene-like WS_2 nanostructures. For $\lambda_{\text{exc}} = 514 \text{ nm}$, it is remarkable that the intensity of the strongest second-order Raman peak, the $2\text{LA}(\text{M})$ mode at 352 cm^{-1} , is approximately twice the intensity of the first-order $A_{1g}(\Gamma)$. Although the $2\text{LA}(\text{M})$ mode overlaps with the first-order $E_{2g}^1(\Gamma)$ mode at 356 cm^{-1} , the multi-peak Lorentzian fitting shown in Figure 1e clearly separates their individual contributions.

The samples contain a large number of monolayer islands (1L), plus enough multilayer islands (see Figure 2a) to study the thickness dependence of the Raman response. The AFM height profile shown in Figure 2e confirms the presence of one and few-layered regions within a single island. Raman mapping of this island at $\lambda_{\text{exc}} = 514 \text{ nm}$ provides spatial maps of the $2\text{LA}(\text{M})$ intensity and the $A_{1g}(\Gamma)$ mode frequency and intensity, as shown in Figures 2b,c,d. The absolute intensity of the $2\text{LA}(\text{M})$ mode increases with decreasing the number of layers, while the intensity of the $A_{1g}(\Gamma)$ displays the opposite behavior. The softening of the $A_{1g}(\Gamma)$ mode with decreasing number of layers (depicted in Figures 2c, e) presumably results from weaker interlayer contributions to the phonon restoring forces.

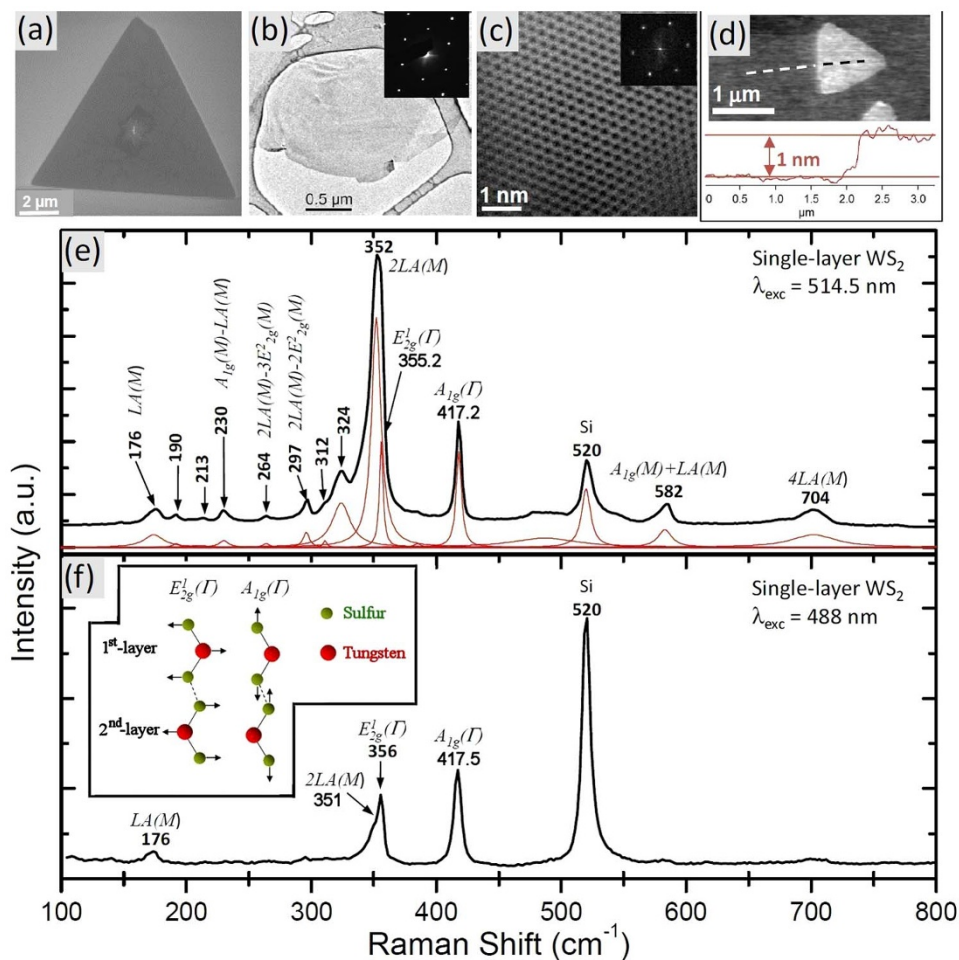


Figure 1 | (a) SEM image of a monolayer WS_2 triangular island. (b) TEM image of a WS_2 island transferred to a lacey carbon grid with inset showing the electron diffraction pattern of the entire region. (c) High-resolution phase-contrast TEM image showing the hexagonal arrangement of the WS_2 structure with inset showing the Fourier transform of the micrograph. (d) AFM image of a WS_2 island and the corresponding height profile along the dashed line. (e) and (f) Room-temperature Raman spectra from a monolayer WS_2 region, using the 514.5 and 488 nm laser excitation, respectively, including Lorentzian peak fits for 514.5 nm data. The inset in (f) shows the atomic displacements for the in-plane phonon mode $E_{2g}^1(\Gamma)$ and the out-of-plane phonon mode $A_{1g}(\Gamma)$ for two adjacent layers, the dashed line represents the weak inter-layer van der waals interaction.

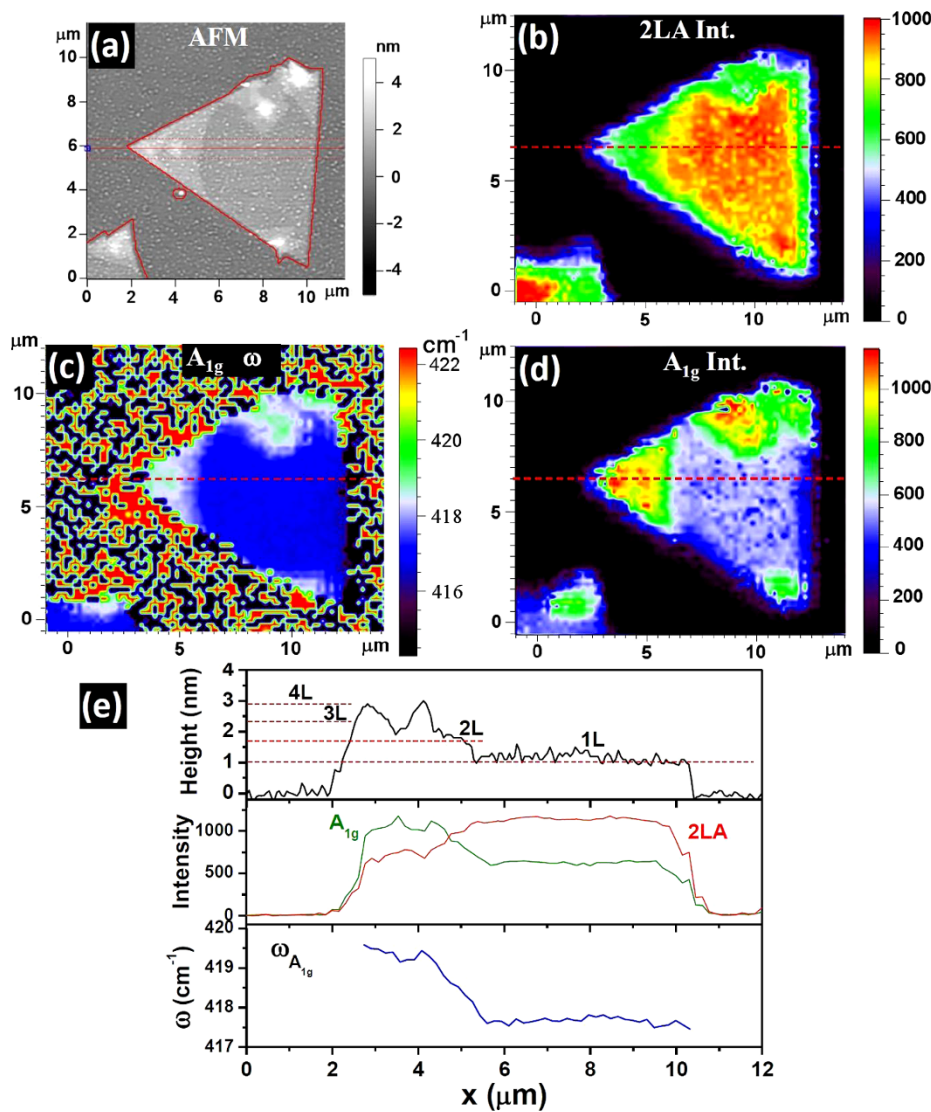


Figure 2 | (a) AFM image of a WS₂ triangular island, which varies from four to one layers thick. Also Raman mappings of the same WS₂ island (using 514.5 nm laser excitation): (b) intensity of the 2LA second-order mode, (c) frequency and (d) intensity of the A_{1g} mode. (e) Line profiles along the red horizontal line in each image corresponding to height, 2LA intensity, A_{1g} intensity and A_{1g} peak position (ω). The Raman mappings as well as the intensity profiles refer to the maximum intensity of the peaks (not the integrated intensities).

Figure 3 summarizes the WS₂ Raman spectra as a function of island thickness and excitation wavelength. For $\lambda_{\text{exc}} = 647$ nm, the absolute intensity of all Raman modes increases with the number of layers, which suggests that at this wavelength the Raman intensity is mainly affected by the scattering volume. A baseline related to the low-energy tail of the photoluminescence (which is centered around 630 nm²⁰) appears for 3L and becomes more obvious in thinner samples. As reported in a previous work²⁰, room-temperature PL is associated with a transition from indirect-gap few-layer WS₂ to direct-gap monolayer WS₂. Raman spectra taken with $\lambda_{\text{exc}} = 488$ nm also showed an increase in the absolute intensity from 1L to 3L. However, the intensities for bulk are lower than for the 1L case. Such a behavior has been previously observed in graphene³¹ and MoS₂¹³ deposited on SiO₂/Si substrates and is mainly attributed to optical interference in both the excitation laser and the Raman signal emitted by the sample. In contrast to these relatively familiar behaviors, the response at $\lambda_{\text{exc}} = 514.5$ nm is a special case: the second-order Raman peaks, in particular the 2LA(M) mode, *increase* in intensity with decreasing number of layers and reach a maximum for the monolayer.

We performed multi-peak Lorentzian fittings on each spectrum to obtain the thickness-dependent frequency of the main WS₂ Raman peaks (2LA(M), E¹_{2g}(Γ) and A_{1g}(Γ)) for each wavelength, as shown in Figure 4a. The A_{1g}(Γ) mode blueshifts when increasing the number of WS₂ layers. This hardening of the A_{1g} mode is consistent with the increasing restoring force caused by van der Waals interactions established among layers, and it is in agreement with previous results reported for MoS₂¹⁸. The E¹_{2g}(Γ) and 2LA(M) phonon modes, however, exhibit very subtle redshifts when increasing the number of layers. It is worth noticing that in WS₂, the close proximity of the 2LA(M) and E¹_{2g}(Γ) increases the error in determining the frequency shift of both modes. The change in frequency is of the order of magnitude of the error bar, which is also affected by the fitting process, thus making more difficult to establish a clear frequency dependence with the number of layers. An anomalous behavior of the E¹_{2g}(Γ) mode has been previously reported in few-layered MoS₂ films^{13,18,24} and it might be caused by a stronger dielectric screening of the long-range Coulomb interactions between the effective charges in thicker samples²⁵. A change in dielectric screening with the number of layers is also expected for WS₂.

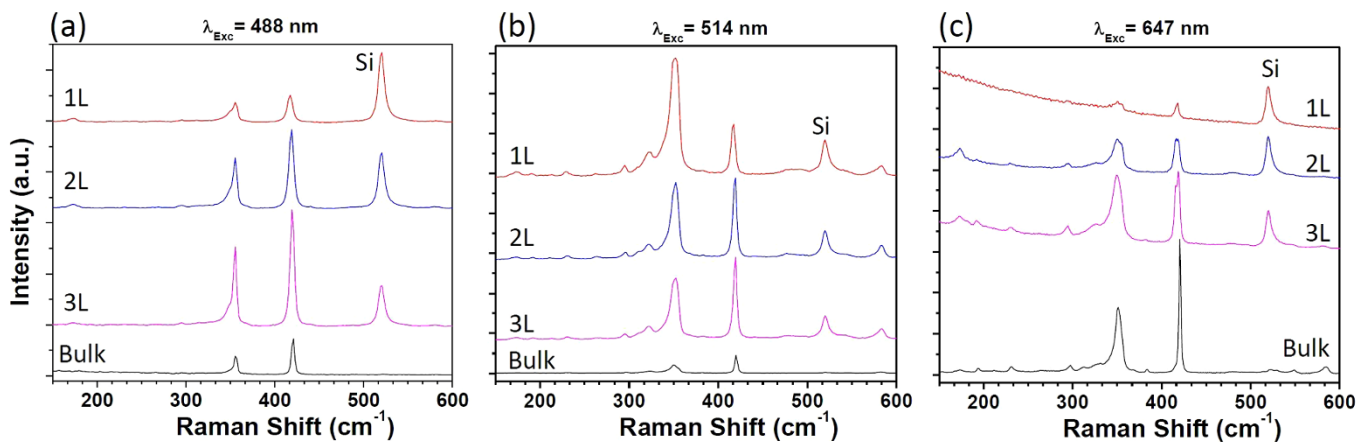


Figure 3 | Raman spectra collected from regions with different WS_2 thicknesses (1L, 2L, 3L and bulk) using three different excitation wavelengths: (a) 488 nm , (b) 514.5 nm and (c) 647 nm . For each individual wavelength all the spectra, including that from the bulk, were acquired using the same experimental conditions of laser power and collection time.

We also studied the relative intensities of the strongest Raman peaks for each λ_{exc} as a function of the number of layers, as shown in Figure 4b. For $\lambda_{\text{exc}} = 488 \text{ nm}$ and $\lambda_{\text{exc}} = 647 \text{ nm}$, the most intense features in the Raman spectrum correspond to the $E_{2g}^1(\Gamma)$ and $A_{1g}(\Gamma)$ modes and the intensity ratio $I_{E_{2g}^1}/I_{A_{1g}}$ does not show major changes with the number of layers. The most interesting scenario again occurs for $\lambda_{\text{exc}} = 514.5 \text{ nm}$. In this case, the strongest Raman peaks are those associated with the 2LA(M) and $A_{1g}(\Gamma)$ phonon modes. The relative intensity $I_{2\text{LA}}/I_{A_{1g}}$ increases dramatically for double- and single-layered films. We have repeated the experiment in different regions of the samples and also in WS_2 films suspended on a TEM grid; the ratio $I_{2\text{LA}}/I_{A_{1g}}$ is always larger than 2 only for monolayer films; thus it provides an accurate fingerprint for monolayer WS_2 . We attribute the intense 2LA signal in monolayer WS_2 at $\lambda_{\text{exc}} = 514.5 \text{ nm}$ to a double-resonant (DR) Raman process which is possible only in the specific electronic band structure of the monolayer, as described below.

Table 1 summarizes the frequency for the main Raman modes as well as the intensity ratio for the most intense peaks, as a function of the number of layers and the excitation wavelength.

Discussion

Figure 5 shows the phonon dispersion and electronic band structures for bulk and monolayer WS_2 , obtained using the density functional perturbation theory in the local density approximation. The experimental Raman peak at 176 cm^{-1} falls in the range of the calculated zone-edge acoustic phonons. This mode has been identified with the longitudinal acoustic mode around the M point of the Brillouin zone^{28,30}, although an alternative identification with the K point has been proposed by at least one group²⁹. This finite-wavevector mode is presumably activated by disorder to become Raman active²⁸. The precise doubling of frequency for the peak at 352 cm^{-1} strongly suggests that such a peak is a second-order mode originated from the same phonon. The unique sensitivity of second-order resonant

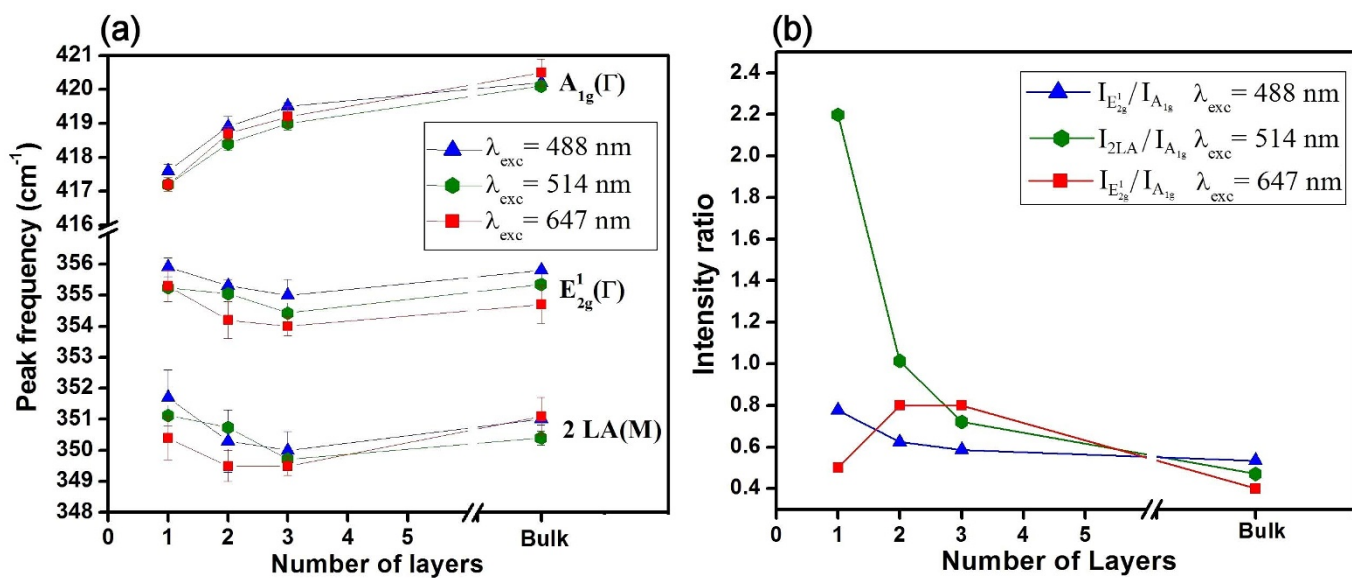


Figure 4 | Intensity ratios and peak frequencies of WS_2 Raman modes. (a) Frequencies of the A_{1g} , E_{2g}^1 , and 2LA Raman modes as a function of thickness (number of WS_2 monolayers) for the three excitation laser lines. Each point represents an average over ten different positions and the error bars correspond to the standard deviations (b) Thickness-dependent intensity ratios of $I_{2\text{LA}}/I_{A_{1g}}$ (for $\lambda_{\text{exc}} = 514.5 \text{ nm}$) and $I_{E_{2g}^1}/I_{A_{1g}}$ (for $\lambda_{\text{exc}} = 488$ and 647 nm).



Table 1 | Summary of the frequency for the main Raman modes as well as the intensity ratio for the most intense peaks, as a function of the number of layers and the excitation wavelength

λ_{Exc}	Phonon modes	1-layer	2-layers	3-layers	Bulk
488 nm	$A_{1g}(\Gamma) \text{ (cm}^{-1}\text{)}$	417.5	418.9	419.5	420.2
	$E_{2g}^1(\Gamma) \text{ (cm}^{-1}\text{)}$	355.9	355.3	355	355.8
	$2LA(M) \text{ (cm}^{-1}\text{)}$	351.7	350.3	350	351
	$I_{E_{2g}^1}/I_{A_{1g}}$ (Intensity ratio)	0.78	0.62	0.59	0.53
514.5 nm	$A_{1g}(\Gamma) \text{ (cm}^{-1}\text{)}$	417.2	418.4	419	420.1
	$E_{2g}^1(\Gamma) \text{ (cm}^{-1}\text{)}$	355.2	355	354.4	355.3
	$2LA(M) \text{ (cm}^{-1}\text{)}$	351.1	350.7	349.7	350
	$I_{2LA}/I_{A_{1g}}$ (Intensity ratio)	2.2	1.01	0.72	0.47
647 nm	$A_{1g}(\Gamma) \text{ (cm}^{-1}\text{)}$	417.2	418.7	419.2	420.5
	$E_{2g}^1(\Gamma) \text{ (cm}^{-1}\text{)}$	355.3	354.2	354	354.7
	$2LA(M) \text{ (cm}^{-1}\text{)}$	350.4	349.5	349.5	351.1
	$I_{E_{2g}^1}/I_{A_{1g}}$ (Intensity ratio)	0.5	0.8	0.8	0.4

Raman processes to precise phonon wavevectors enables us to unambiguously identify the second-order 352 cm^{-1} peak (and by extension, the first-order 176 cm^{-1} peak) with the M-point LA phonon, as described below.

The double resonant Raman process involves two phonons with equal and opposite momentum and an intermediate excited electronic state that resonates with the electronic band structure (in

addition to the resonance for the initial optical transition, hence the term double resonance). For a second-order Raman process to satisfy the requirements for double resonance, the optical excitation energy must match a vertical electronic transition (vertical black arrows in Figure 6) and the conduction band must contain quasi-isoenergetic electronic states (dashed red arrows in Figure 6) at a momentum difference corresponding to the phonon momentum $\pm q$

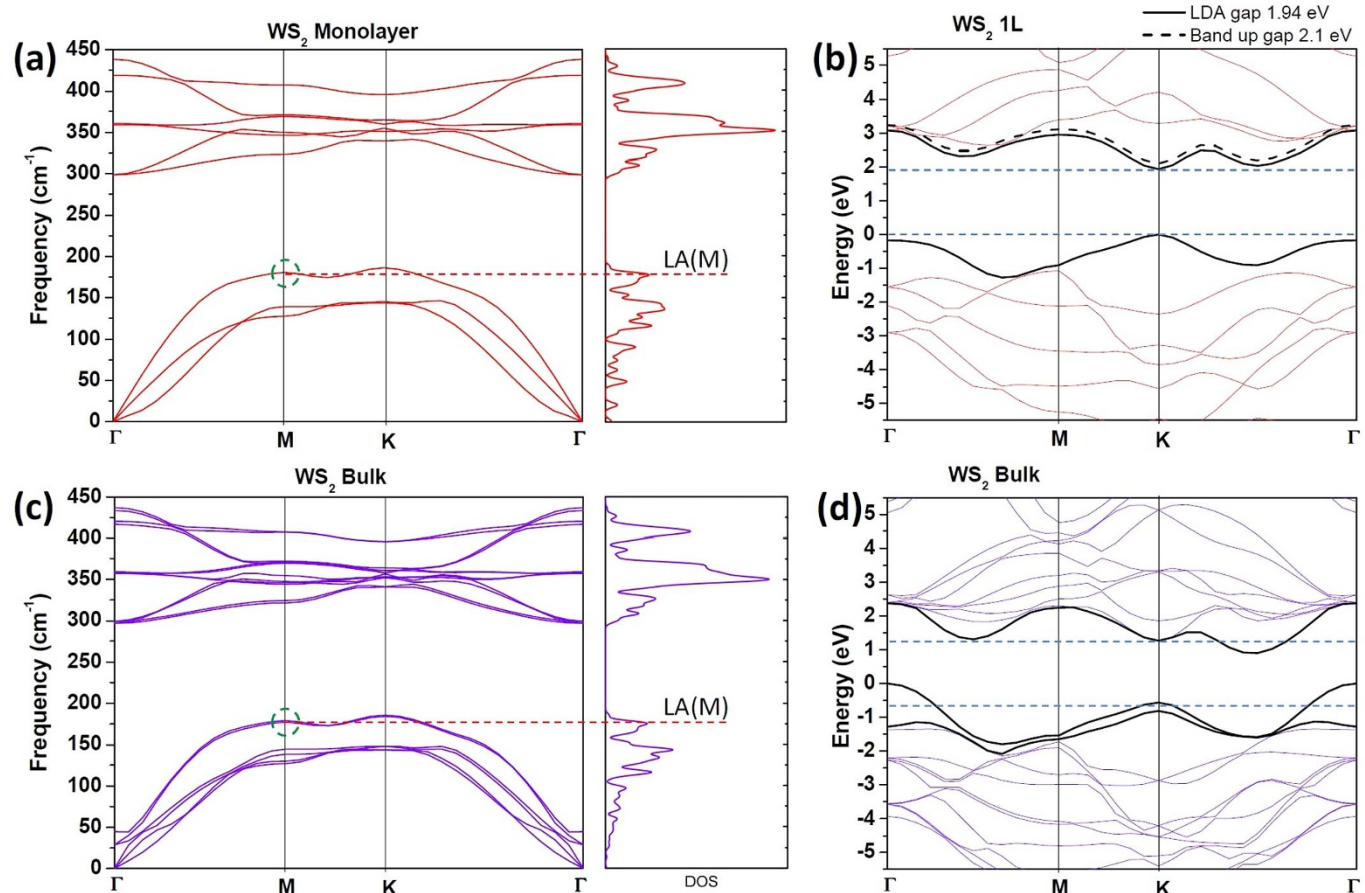


Figure 5 | Phonon dispersion plus density of states [left]; and electronic band structures [right] for WS_2 monolayer [top] and bulk [bottom], respectively. The electronic band structure in (b) was calculated by LDA with 1.94 eV band gap; the dashed line corresponds to the bottom of the conduction band with a rigid shift to match the experimental 2.1 eV band gap. Although the phonon dispersions for monolayer and bulk are very similar, their band structures are clearly different. While the direct gap at the K point remains almost the same; the electronic bands between Γ -M and Γ -K undergo major changes associated with the indirect-to-direct bandgap transition from bulk to monolayer. The horizontal dashed lines in (b) and (d) are guides for the eye to visualize better these differences.

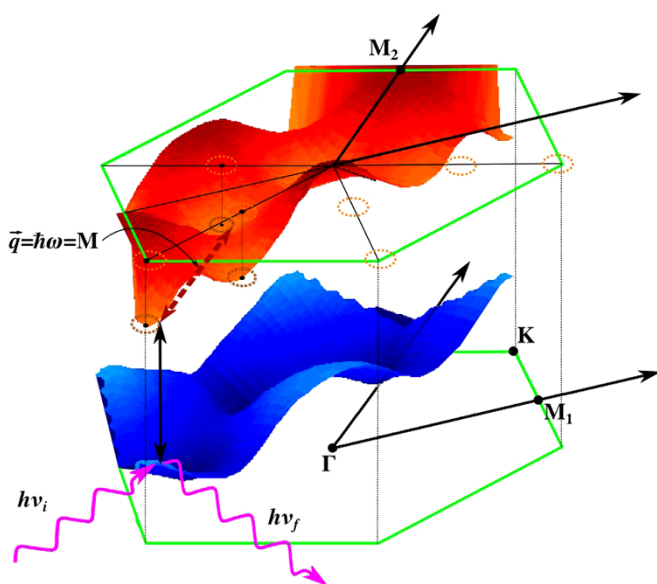


Figure 6 | Schematic of the double-resonant Raman process that generates the 2LA(M) experimental peak. Calculated data from the valence (blue) and conduction (red) bands are used for the visualization. An incident photon with energy $h\nu_i$ produces a vertical electronic transition (black vertical arrow) from valence to conduction band. The electron in the conduction band then experiences two electron-phonon scattering events, the first scattering event involving a phonon with momentum $+q$ and the second involving a phonon with momentum $-q$ (red dashed double arrow). Finally another vertical transition from conduction to valence band emits a Raman-shifted photon with energy $h\nu_f$.

(or similarly for the valence band in the case of phonon-hole scattering). The momentum dependence of the electronic structure and phonon dispersion must combine to produce sharp peaks in momentum space for the double resonant process, in order to produce a sharp Raman feature.

Since the most important structure in the double-resonant process typically arises from the complex interplay of electron and phonon dispersion relations, the essential features of double-resonant Raman processes can be captured in a ‘reduced’ calculation under a simplifying assumption of constant scattering matrix elements for the component scattering events. Thus the *ab initio* electronic and phonon band structures can be used to compute the reduced intensity of the 2LA mode from the fourth-order Fermi golden rule – for details, see the Methods section. The numerical results corresponding to this model are summarized in Figure 7, where the reduced intensity of the 2LA double resonant mode at different q -points is plotted as a function of the laser wavelength. The reduced intensities for the bulk and the monolayer were investigated in the vicinity of the three laser excitations: 488, 514.5 and 647 nm. At 488 and 647 nm the Raman intensity of the bulk is always greater than the monolayer (not shown). However, the monolayer exhibits a pronounced resonant peak close to 514.7 nm. Furthermore, by restricting the phonon wavevectors allowed in the calculation, it is possible to clearly identify the reciprocal space location of the dominant phonon contributions to the double resonance. In particular, Figure 7 compares the contributions from phonons in the vicinity of K and M; the dominance of the M-point contribution is obvious, which justifies the identification of this process with 2LA(M).

In the bulk system, changes in the electronic structure drive the system out of resonance for both electron-phonon and hole-phonon mediated processes. By comparing Figure 5(b) and 5(d) it can be observed that the direct band gap at the K point is similar for both bulk and monolayer WS₂. However, the electronic bands between Γ -

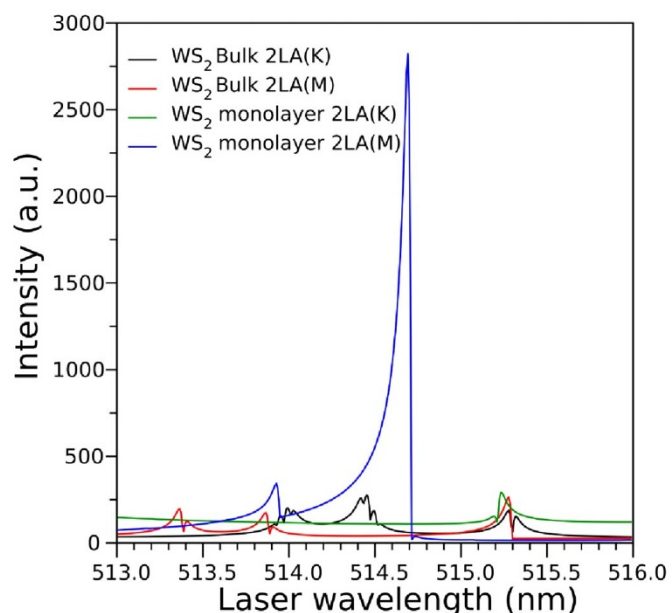


Figure 7 | Reduced Raman intensity of the 2LA Raman line at the vicinity of K and M as a function of laser energy using a double-resonant model for both bulk and monolayer WS₂. Although the reduced intensities were also investigated around 488 and 647 nm (not shown), the monolayer system shows a resonant peak only for the vicinity of 514.7 nm.

M and Γ -K exhibit major differences, which reveal an indirect to direct band gap material transformation when the system transitions from bulk to monolayer. This tendency persisted after a small rigid shift of the conduction band was applied to correct the well-known DFT underestimation of the band gap and match the experimental gap of 2.1 eV³², which is similar to the GW-corrected direct gap of 2.1 eV³³.

In summary, we have systematically studied the thickness- and wavelength-dependent Raman behavior for newly synthesized single- and few-layered two-dimensional WS₂ crystals. Our results reveal that the A_{1g}(Γ) mode softens while the 2LA(M) and E_{12g}(Γ) modes present a very subtle hardening with decreasing number of WS₂ layers. The analysis presented here unambiguously confirms that the 176 cm⁻¹ feature arises from an M-point phonon. In addition, a striking increase in the intensity of the 2LA(M) mode occurs with 514 nm laser excitation. This behavior can be explained in terms of a double resonance process which is active only in the monolayer. Both frequency shifts and changes in relative intensity can provide an unambiguous, nondestructive identification of monolayer WS₂. The more singular dispersion relations of electrons and phonons in two dimensions (as compared to three) facilitate the generation of sharp Raman features via a complex double-resonant process. This mechanism may be more broadly applicable in characterizing the structural, electronic and vibrational properties of other layered systems.

Methods

Synthesis. WO₃ thin films (5–20 Å) were thermally deposited on SiO₂/Si substrates in high vacuum (10^{-5} – 10^{-6} Torr). Subsequently, the films were transferred into a quartz tube reactor. During the sulfurization of the WO₃ films, samples were kept at 800 °C for 30 min under an Argon flow and S vapors were generated from S powders placed up-stream in a lower temperature region (~250 °C) which was independently controlled.

For the TEM observations, we transferred as-grown WS₂ islands onto gold Quantifoil® TEM grids (from SPI), which contain a polymer thin film with 2 μm periodic holes. The WS₂ islands were released from the original Si/SiO₂ wafer by two methods, both of which involved etching in 15 M KOH. The first approach³⁴ spin-coats the wafer with a PMMA solution (495k) at 3000 RPM for 30 seconds. The polymer was then allowed to cure overnight at room temperature. The edge of the



wafer was marked with a sharp blade to expose the Si/SiO₂ surface and the wafer was subsequently immersed in 15 M KOH. The PMMA/WS₂ film was released by the effect of the caustic solution and could be fished out with the TEM grid. The TEM grid was then placed on absorbent paper and thoroughly washed with deionized water. Finally, the PMMA was dissolved with acetone droplets. In an alternative PMMA-free approach³⁵, the TEM grid was placed on the Si/SiO₂ wafer containing the WS₂ islands. One drop of IPA was allowed to dry on the TEM grid and after 10 minutes the wafer was immersed in 15 M KOH. The grid was released and placed on absorbent paper and washed thoroughly with deionized water.

Characterization. WS₂ films were characterized by Raman and PL spectroscopies performed in a Renishaw inVia confocal microscope-based Raman spectrometer with a spectral resolution better than 1 cm⁻¹. We used 488, 514.5 and 647 nm laser excitations, keeping the laser power under 0.2 mW at all times. The 520 cm⁻¹ phonon mode from the silicon substrate was used for calibration. The Raman spectra for the bulk were collected from WS₂ powder, 99% (Sigma-Aldrich). High-resolution transmission electron microscopy was carried out in a JEOL 2010F equipped with an energy dispersive X-ray (EDX) spectrometer, with an accelerating voltage of 200 kV, field-emission source, ultra-high resolution pole piece (Cs = 0.5 mm), and a 1.9 Å Scherzer limit. SEM observations were performed in a FEI XL30 SEM at 6 kV and an LEO 1530 FESEM operated at 1 kV. Non-contact atomic force microscopy was performed in a MFP-3D-SA from Asylum Research.

Theoretical modeling. Electronic structure calculations are carried out using density functional theory in the local density approximation, with the Ceperley and Adler exchange correlation functional parametrized by Perdew and Zunger, as implemented in the plane-wave code CASTEP³⁶ within Materials Studio 5.5 (software by Accelrys at accelrys.com). The structures are geometrically optimized until the energy difference reached 5×10^{-6} eV/atom with a maximum force of 0.01 eV/Å. The plane wave cutoff energy was 720 eV with a norm-conserving pseudopotential on a grid of $9 \times 9 \times 2$ k-points and a FFT grid of $30 \times 30 \times 108$ for the WS₂ crystal and $30 \times 30 \times 180$ for the WS₂ isolated layer; (the WS₂ layer has a larger cell in the c direction). The phonon density of states and dispersion curves were calculated with the above parameters using density functional perturbation theory as implemented in CASTEP, using a linear response methodology that works well for insulators³⁷.

The optimized unit cell lattice parameters for the WS₂ crystal are $a = b = 3.147\text{ \AA}$ and $c = 12.167\text{ \AA}$, while the experimental values reported are: $a = b = 3.153\text{ \AA}$ and $c = 12.323\text{ \AA}$.³⁸ For the WS₂ monolayer, the calculated a and b parameters ($a = b = 3.146\text{ \AA}$) are almost the same as those for the bulk crystal. The distance between the layers is set to 20 Å to eliminate interlayer interaction.

The double resonant Raman reduced intensities of the 2LA mode were modeled using the Fermi golden rule generalized to fourth order²⁷. Electron-two-phonon-electron, electron-two-phonon-hole, and hole-two-phonon-hole processes were considered. The scattering matrix elements were held constant, so that, one summand of I^{pp} of the electron-electron two-phonon process is expressed as:

$$\frac{1}{N_k N_q N_c N_v N_a N_\beta} \sum_{k,q,c,v,a,\beta} \frac{1}{\left(\epsilon_L - \epsilon_k^c + \epsilon_k^v - \hbar\omega_{-q}^a - \hbar\omega_q^\beta - i\frac{\gamma}{2} \right) \left(\epsilon_L - \epsilon_{k+q}^c + \epsilon_k^v - \hbar\omega_{-q}^a - i\frac{\gamma}{2} \right) \left(\epsilon_L - \epsilon_k^c + \epsilon_k^v - i\frac{\gamma}{2} \right)}$$

The sum is over k-points k , q-points q , valence bands v , conduction bands c and phonon branches a and β . For the bulk WS₂ structure, 234 k-points were used to sample the Brillouin zone, the three highest valence bands, the three lowest conduction bands, and two phonon branches over 24 q-points. For monolayer WS₂, 234 k-points were also used to sample the Brillouin zone, the two highest valence bands, the two lowest conduction bands, and one phonon branch over 12 q-points. The reduced intensity is computed as the sum over all possible processes using the density functional theory band structure after a small rigid shift was applied to the conduction bands to account for the well-known underestimation of the calculated band gap within DFT. Only the electron-two-phonon-electron processes are found to contribute significantly to the difference in intensity between the monolayer and the bulk.

1. Geim, A. K. & Novoselov, K. S. The rise of graphene. *Nature Materials* **6**, 183–191 (2007).
2. Novoselov, K. S. Graphene: Materials in the Flatland (Nobel Lecture). *Angewandte Chemie-International Edition* **50**, 6986–7002 (2011).
3. Ci, L. et al. Atomic layers of hybridized boron nitride and graphene domains. *Nature Materials* **9**, 430–435 (2010).
4. Jin, C. H., Lin, F., Suenaga, K. & Iijima, S. Fabrication of a Freestanding Boron Nitride Single Layer and Its Defect Assignments. *Physical Review Letters* **102** (2009).
5. Albe, K. & Klein, A. Density-functional-theory calculations of electronic band structure of single-crystal and single-layer WS₂. *Physical Review B* **66** (2002).
6. Ding, Y. et al. First principles study of structural, vibrational and electronic properties of graphene-like MX(2) (M = Mo, Nb, W, Ta; X = S, Se, Te) monolayers. *Physica B-Condensed Matter* **406**, 2254–2260 (2011).
7. Ma, Y. D. et al. Electronic and magnetic properties of perfect, vacancy-doped, and nonmetal adsorbed MoSe(2), MoTe(2) and WS(2) monolayers. *Physical Chemistry Chemical Physics* **13**, 15546–15553 (2011).

8. Mak, K. F., Lee, C., Hone, J., Shan, J. & Heinz, T. F. Atomically Thin MoS(2): A New Direct-Gap Semiconductor. *Physical Review Letters* **105** (2010).
9. Splendiani, A. et al. Emerging Photoluminescence in Monolayer MoS(2). *Nano Letters* **10**, 1271–1275 (2010).
10. Xiao, D., Liu, G. B., Feng, W. X., Xu, X. D. & Yao, W. Coupled Spin and Valley Physics in Monolayers of MoS₂ and Other Group-VI Dichalcogenides. *Physical Review Letters* **108**, 196802 (2012).
11. Cao, T. et al. Valley-selective circular dichroism of monolayer molybdenum disulphide. *Nature Communications* **3**, DOI: 10.1038/ncomms1882 (2012).
12. Eda, G. et al. Photoluminescence from Chemically Exfoliated MoS(2). *Nano Letters* **11**, 5111–5116 (2011).
13. Lee, C. et al. Anomalous Lattice Vibrations of Single- and Few-Layer MoS(2). *Acs Nano* **4**, 2695–2700 (2010).
14. Matte, H. S. S. R. et al. MoS(2) and WS(2) Analogues of Graphene. *Angewandte Chemie-International Edition* **49**, 4059–4062 (2010).
15. Radisavljevic, B., Radenovic, A., Brivio, J., Giacometti, V. & Kis, A. Single-layer MoS₂ transistors. *Nature Nanotechnology* **6**, 147–150 (2011).
16. Yin, Z. Y. et al. Single-Layer MoS₂ Phototransistors. *ACS Nano* **6**, 74–80 (2012).
17. Zhan, Y., Liu, Z., Najmaei, S., Ajayan, P. M. & J. L. Large-Area Vapor-Phase Growth and Characterization of MoS₂ Atomic Layers on a SiO₂ Substrate. *Small* **8**, 966–971 (2012).
18. Li, H. et al. From Bulk to Monolayer MoS₂: Evolution of Raman Scattering. *Advanced Functional Materials* **22**, 1385–1390 (2012).
19. Lee, Y. H. et al. Synthesis of Large-Area MoS₂ Atomic Layers with Chemical Vapor Deposition. *Advanced Materials* **24**, 2320–2325 (2012).
20. Gutierrez, H. R. et al. Extraordinary room-temperature photoluminescence in WS₂ monolayers. *Nano Letters* **12**, 3026357 (2012).
21. Ferrari, A. C. et al. Raman spectrum of graphene and graphene layers. *Physical Review Letters* **97** (2006).
22. Gupta, A., Chen, G., Joshi, P., Tadigadapa, S. & Eklund, P. C. Raman scattering from high-frequency phonons in supported n-graphene layer films. *Nano Letters* **6**, 2667–2673 (2006).
23. Yoon, D. et al. Variations in the Raman Spectrum as a Function of the Number of Graphene Layers. *Journal of the Korean Physical Society* **55**, 1299–1303 (2009).
24. Najmaei, S., Liu, Z., Ajayan, P. M. & Lou, J. Thermal effects on the characteristic Raman spectrum of molybdenum disulfide (MoS₂) of varying thicknesses. *Applied Physics Letters* **100**, 013106 (2012).
25. Molina-Sanchez, A. & Wirtz, L. Phonons in single-layer and few-layer MoS₂ and WS₂. *Physical Review B* **84**, 155413 (2011).
26. Gorbachev, R. V. et al. Hunting for Monolayer Boron Nitride: Optical and Raman Signatures. *Small* **7**, 465–468 (2011).
27. Venezuela, P., Lazzeri, M. & Mauri, F. Theory of double-resonant Raman spectra in graphene: Intensity and line shape of defect-induced and two-phonon bands. *Physical Review B* **84**, 035433 (2011).
28. Frey, G. L., Tenne, R., Matthews, M. J., Dresselhaus, M. S. & Dresselhaus, G. Optical properties of MS₂ (M = Mo, W) inorganic fullerene-like and nanotube material optical absorption and resonance Raman measurements. *Journal of Materials Research* **13**, 2412–2417 (1998).
29. Sourisseau, C., Cruge, F., Fouassier, M. & Alba, M. 2Nd-Order Raman Effects, Inelastic Neutron-Scattering and Lattice-Dynamics in 2H-Ws₂. *Chemical Physics* **150**, 281–293 (1991).
30. Stacy, A. M. & Hodul, D. T. Raman-Spectra of Ivb and Vib Transition-Metal Disulfides Using Laser Energies near the Absorption Edges. *Journal of Physics and Chemistry of Solids* **46**, 405–409 (1985).
31. Wang, Y. Y., Ni, Z. H., Shen, Z. X., Wang, H. M. & Wu, Y. H. Interference enhancement of Raman signal of graphene. *Applied Physics Letters* **92**, 043121 (2008).
32. Beal, A. R. & Liang, W. Y. Excitons in 2H-Wse2 and 3R-Ws2. *Journal of Physics C-Solid State Physics* **9**, 2459–2466 (1976).
33. Jiang, H. Electronic Band Structures of Molybdenum and Tungsten Dichalcogenides by the GW Approach. *Journal of Physical Chemistry C* **116**, 7664–7671 (2012).
34. Reina, A. et al. Large Area, Few-Layer Graphene Films on Arbitrary Substrates by Chemical Vapor Deposition. *Nano Letters* **9**, 30–35 (2009).
35. Regan, W. et al. A direct transfer of layer-area graphene. *Applied Physics Letters* **96**, 113102 (2010).
36. Clark, S. J. et al. First principles methods using CASTEP. *Zeitschrift Fur Kristallographie* **220**, 567–570 (2005).
37. Refson, K., Tulip, P. R. & Clark, S. J. Variational density-functional perturbation theory for dielectrics and lattice dynamics. *Physical Review B* **73**, 155114 (2006).
38. Schutte, W. J., Deboer, J. L. & Jellinek, F. Crystal-Structures of Tungsten Disulfide and Diselenide. *Journal of Solid State Chemistry* **70**, 207–209 (1987).

Acknowledgements

M.T., H.R.G., A.L.E. and V.H.C. acknowledge funding from the U.S. Army Research Office MURI grant W911NF-11-1-0362. This research was partially supported by the Materials Simulation Center of the Materials Research Institute, the Research Computing and Cyberinfrastructure unit of Information Technology Services. MT acknowledges JST-Japan for funding the Research Center for Exotic NanoCarbons, under the Japanese regional Innovation Strategy Program by the Excellence. M.T. and V.H.C. also acknowledge support



from a Penn State Center for Nanoscale Science Seed grant on 2-D Layered Materials (DMR-0820404). This publication was also supported by the Pennsylvania State University Materials Research Institute Nanofabrication Lab and the National Science Foundation Cooperative Agreement No. ECS-0335765. Electron microscopy characterization facilities within the Materials Research Institute at the Pennsylvania State University were also used for this research. A.R.B.M. and J.-C.C. acknowledge financial support from the F.R.S.-FNRS of Belgium. This research is directly connected to the ARC on « Graphene StressTronics » sponsored by the Communauté Française de Belgique.

Author contributions

M.T., H.T. and H.R.G. designed the experiments. The synthesis of the samples was carried out by N.P.L., H.R.G. and A.L.E. The Raman spectra were acquired by A.B. and H.R.G. Theoretical calculations were performed by H.T., F.L.U., A.R.B.M., J.-C.C., V.C. and C.-I.C.

AFM characterization was performed by B.W. and H.R.G. TEM sample preparation was carried out by A.L.E. and H.R.G. TEM observations were carried out by H.R.G. SEM characterization was carried out by A.L.E. and N.P.L. All the authors contributed to the manuscript preparation and discussion of results.

Additional information

Competing financial interests: The authors declare no competing financial interests.

License: This work is licensed under a Creative Commons Attribution-NonCommercial-NoDerivs 3.0 Unported License. To view a copy of this license, visit <http://creativecommons.org/licenses/by-nc-nd/3.0/>

How to cite this article: Berkdemir, A. *et al.* Identification of individual and few layers of WS₂ using Raman Spectroscopy. *Sci. Rep.* 3, 1755; DOI:10.1038/srep01755 (2013).